Supplementary information for "A microfluidic method for controlled generation and trapping of membraneless water-in-water droplets"

Chi Li[a,b†], Hailin Fu[c,d*†], Kalpit J. Bakal[a,b], Jaap M.J. den Toonder[a,b,d], E. W. Meijer[c,d], Sailing He[a*], Hans M. Wyss[a,b,d*]

[1] IDEAS ZJU-TU/e Joint Research Institute of Design, Optoelectronics and Sensing, College of Optical Science and Engineering, Zhejiang University 866 Yuhangtang Road, Hangzhou, 310058, Zhejiang, China.
[2] Life Sciences Institute, Zhejiang University 866 Yuhangtang Road, Hangzhou, 310058, Zhejiang, China.
[3] Department of Mechanical Engineering, Eindhoven University of Technology, De Zaale 5, Eindhoven, 5612 AE, The Netherlands.
[4] Institute for Complex Molecular Systems (ICMS), Eindhoven University of Technology, de Zaale 5, Eindhoven, 5612 AE, The Netherlands.
[a] IDEAS ZJU-TU/e Joint Research Institute of Design, Optoelectronics and Sensing, College of Optical Science and Engineering, Zhejiang University 866 Yuhangtang Road, Hangzhou, 310058, Zhejiang, China.
Email: sailing@zju.edu.cn
[b] Department of Mechanical Engineering, Eindhoven University of Technology, De Zaale 5, Eindhoven, 5612 AE, Noord Brabant, The Netherlands.
Email: H.M.Wyss@tue.nl
[c] Department of Chemistry and Chemical Engineering and Laboratory of Macromolecular and Organic Chemistry, Eindhoven University of Technology, De Zaale 5, Eindhoven, 5612 AE, Noord Brabant, The Netherlands.
Email: h.fu@tue.n l
[d] Institute for Complex Molecular Systems (ICMS), Eindhoven University of Technology, De Zaale 5, Eindhoven, 5612 AE, Noord Brabant, The Netherlands.
†These authors contributed equally to this work.

This PDF file includes:

Supplementary information
Figs. S1 to S8
References (1to 4)

Other Supplementary Materials for this manuscript include the following:

Movies S1 to S8

Supplementary information

PEG-Dextran system

Polyethylene glycol (PEG, MW: 8 kDa) is purchased from Sigma Aldrich. Dextran (MW: 500 kDa) is ordered from Pharmacosmos (Pharmaceutical quality). Dextran-fluorescein isothiocyanate (dextran-FITC, MW: 550 kDa and 110 kDa) and PEG-rhodamine (MW: 10 kDa) are purchased from Creative PEGworks. Water is purified on an EMD Millipore Milli-Q Integral Water Purification system. Pure PEG and pure dextran solutions are prepared by mixing calculated amounts of polymers with milli-Q water and 0.1 to 0.5 mol% of PEG-rhodamine or dextran-FITC for fluorescence imaging.

PAA-PDMAEMA system

Poly(acrylic acid) (PAA, MW: 100 kDa) is purchased from Sigma Aldrich. poly(N,N-dimethylaminoethyl methacrylate) (PDMAEMA, MW: 104 kDa) is ordered from Polymer Source Inc. The mixture solution consisting of 0.28 to 0.33 M of PAA and PDMAEMA each (regarding the monomers) and 1.5 M KCl is adjusted to pH = 6.5 ± 0.2 by adding 1 M hydrochloric acid and 1 M sodium hydroxide to ensure a 1:1 stoichiometric ratio of positive and negative charges. KCl solutions are prepared by mixing the calculated amounts of salts with milli-Q water.

Materials used in femtosecond laser micromachining (FLM)

Potassium hydroxide (45 % KOH) is provided by Sigma Aldrich Inc. as a liquid. The 75 × 25 mm^2 silica wafers with different thicknesses are purchased from SIEGERT WADER Inc., including the thicknesses of 1 mm, 0.5 mm, and 0.2 mm. Different thickness wafers are adapted for different imaging lenses.

Materials used in PDMS-based microfluidic chip fabrication

10 cm diameter silica wafers are purchased from SIEGERT WADER Inc., and SU-8 2000 is purchased from MicroChem Inc.

Femtosecond laser micromachining (FLM)

We use an instrument from FEMTOprint Int. For the fabrication, the wavelength, repetition rate, single pulse energy, and objective lens are 1026 nm, 200 kHz, 230 nJ, and 20 X, respectively. The machining stages provide a 100-nanometer moving resolution and 2 mm/s processing speed is used in this work, more details can be found in Supporting information S1.

The region modified by a femtosecond laser beam can be etched through hydrofluoric acid (HF) or potassium hydroxide (KOH). In contrast to HF, KOH exhibits a higher selective etching rate for fused silica, typically around 115 μm /h in the modified region compared to 0.7 μm/h in the bulk material. To ensure a smooth surface and minimize etching time, the sample is initially enclosed within a container and immersed in an ultrasonic water bath heated to 80 ^{o}C. Following the etching process, a thorough cleaning of the samples is performed using acetone and water to remove any residual substances. Consequently, a microfluidic chip featuring an open channel can be successfully fabricated.

Bonding

Fused silica-to-silica bonding is achieved through thermal treatment in a Muffle furnace (L 3/12/C450, from Nabertherm Int.). By increasing the temperature to 1200 ^{o}C and placing a piece of high-temperature resistant ceramic (around 1 kg) on the upper surface of the fused silica, two layers of fused silica are bonded in 8 hours (1000 ^{o}C for 72 hours, experimentally). Fused silica surface bonding with PDMS is performed using a Plasma Asher (Emitech K1050X) with 20-watt treatment power in an oxygen environment.

Filling the device with DI water

A vacuum process is employed to thoroughly fill the microfluidic device with deionized (DI) water, eliminating all air pockets from the channels and chambers of the device. The chip is subsequently attached to the base of a glass beaker using a piece of tape. After securing the device, the container is filled with deionized water to fully submerge the device. The container is subsequently placed in a desiccator, which is linked to a vacuum pump via a tube. Under vacuum conditions, the DI water within the vacuum chamber will start to boil and will reach equilibrium after approximately 10 minutes. Next, we quickly increase the pressure inside the desiccator by swiftly disconnecting the vacuum tube, causing the DI water to rush into the chip through the inlet and outlet, leading to the rapid collapse of any bubbles within the microfluidic channels. While a few bubbles might persist, they can be gradually eliminated by continuously injecting DI water using a syringe pump. Ultimately, the microfluidic chip can be filled with DI water.

Strategy for generating LLPS droplets

After having successfully filled a device with DI water, we employ the following two-step general protocol to create droplets through LLPS within the dead-end chambers of our devices:

In Step 1, a homogeneous solution of compound 1 (dextran in our primary example) is passed through the main channel at a constant flow rate (100 µl/h in our primary example). This flow is accomplished using a syringe pump (HARVARD, PHD ULTRA XF) and applied for a duration of t_1 (t_1=2 hours in our primary example). We typically employ a 1 mL syringe, connected to the device using a Gauge Luer stub (outer diameter of 1.2 mm) and a polyethylene tube with 0.9 and 1.2 mm inner and outer diameter, respectively. The presence of compound 1 in the main channel at a fixed concentration leads to the transport of compound 1 into the dead-end chambers of the device. The final concentration of compound or mixture 1 in each dead-end chamber is mainly controlled by the molecular weight, solution viscosity, the applied duration time of t_1, as well as the geometry of the respective junction neck.

In Step 2, a homogeneous solution of compound 2 (PEG in our primary example) is passed through the main channel at a constant flow rate (100 µl/h in our primary example), resulting in the diffusion of compound 2 into the dead-end chambers and the LLPS-induced formation of droplets of compound or mixture 1 in a continuous phase of compound 2 within the dead-end chambers. The flow of compound 2 is typically applied until a quasi-equilibrium is reached, where the concentration of compound 2 in the continuous phase within the chambers matches the concentration applied in the main channel.

Recycling the device

The challenge of reusability has been a persistent issue for PDMS-based microfluidic chips. For the fused silica-based devices presented in this work, this issue can be effectively addressed.

These devices can be effectively re-used by employing the following general protocol: To clean and prepare the chip for re-use, firstly, the PDMS inlet/outlet cover is removed by using a blade in combination with the application of IPA or acetone. Next, the fused silica chip undergoes thermal processing in a muffle furnace set to 800 ^{o}C to remove any remaining polymer residues. The device structure remains unchanged during this process, as the temperature applied is well below the glass transition temperature of fused silica, which is around 1100 ^{o}C. Following the thermal treatment, a new PDMS cover layer with an inlet and outlet is re-bonded to the chip's surface through surface plasma treatment. We consistently apply this recycling method to our microfluidic devices; indeed, each device used in this research has been reused 5 times on average, demonstrating the effectiveness of the applied recycling method.

Microscopic imaging

The high-resolution fluorescent images and movies are acquired with a Leica TCS SP8 microscope in the confocal mode with 10x/0.4 (dry) and 20x/0.75 (dry) objectives at a resolution of 512 × 512 or 1024 × 1024. The lasers used are 488 nm (for FITC) and 552 nm (for rhodamine). The movies are taken with a time gap of 5 or 10 min. The *z*-stack images are collected with a gap of 0.5, 1 or 2 µm. A tile scan with a built-in automatic tilting function is used to obtain a full picture of the microfluidic device. The bright field (white light and fluorescent) images are collected with the Leica TCS SP8 microscope in the BF mode and Nikon microscope.

Femtosecond laser micromachining (FLM) for fused silica device fabrication

The fabrication process for the fused silica-based microfluidic chip can be divided into three steps, as shown in Fig.S1a.

Step 1: We employ the FLM technique to fabricate two silica layers: layer 1 contains the through-hole inlet and outlet, while the main geometry is embedded in layer 2. The regions exposed to femtosecond laser pulses in the focus area of the laser beam undergo structural modifications, resulting in a higher chemical etching rate compared to the bulk area. For the etching step we typically employ a 45 wt% potassium hydroxide (KOH) solution at 85 oC. Under these conditions, the typical etch rate of the exposed regions is around 100 µm per hour; the required etch duration is thus dependent on the geometry of the modified areas.

Step 2: These two layers, after alignment, are bonded together through thermal bonding via a ultra-high temperature treatment in a muffle furnace, either for 72 hours at 1000 oC or for 10 hours at 1200 oC.

Step 3: We use plasma bonding to attach a prepared PDMS layer with an aligned through-hole inlet and outlet to the top surface of layer 1. We use PDMS for this final layer, since the elastic properties of PDMS facilitate the connection of microfluidic tubing that can be readily plugged and unplugged.

The structure of the device, embedded in layer 2, is shown in Fig.S1b; it comprises a main channel, a series of dead-end chambers, and the corresponding connection necks between the main channel and the chambers. The depths of the main channel (hc) and the chambers (hchamb.) are kept the same, at 400 µm, while the depth of the connection necks (hn) is 200 µm, which helps us better control the diffusion across the connection channel to a relatively slow rate and which also makes our fluorescence intensity analysis more convenient; the diameter (Dchamb.) of these chambers is Dchamb. = 300 µm.

Simple model for transport into dead-end chambers by diffusion and diffusio-osmosis

Transport by molecular diffusion

As a starting point, we consider a minimal model in which solute transport into the dead-end chamber is driven solely by molecular diffusion. The system is approximated as two well-mixed reservoirs connected by a narrow neck, as illustrated schematically in Fig. 1.

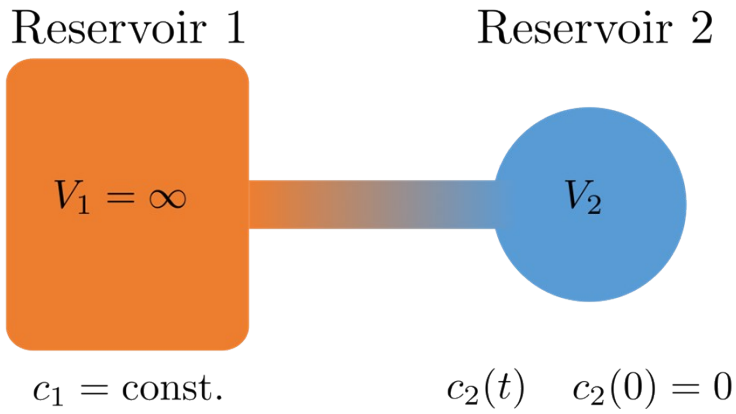

Schematic of the two-reservoir model for diffusion and diffusio-osmosis The main flow channel (Reservoir 1) is maintained at constant dextran concentration c_1, while the dead-end chamber (Reservoir 2) initially contains no solute.

Reservoir 1 represents the main flow channel and is maintained at a constant dextran concentration c_1, while Reservoir 2 corresponds to the dead-end chamber, initially containing no solute.

The two reservoirs are connected by a neck of length $l_n \approx 210\ \mu\text{m}$, width $w_n \approx 30\ \mu\text{m}$, and height $h_n \approx 200\ \mu\text{m}$. The chamber is approximately cylindrical, with diameter $d_c \approx 300\ \mu\text{m}$, height $h_c \approx 400\ \mu\text{m}$, and volume $V_2 = \pi(d_c/2)^2 h_c$.

Assuming perfect mixing within the chamber and a constant linear concentration gradient across the connecting neck, the chamber-averaged concentration evolves according to Fick's law:

$$\frac{dc_2}{dt} = \frac{D\, w_n h_n}{V_2\, l_n}(c_1 - c_2), \qquad c_2(0) = 0,$$

with solution

$$c_2(t) = c_1\left(1 - exp\left[-\frac{D\, w_n h_n}{V_2\, l_n}t\right]\right),$$

where $D \approx 13.7\ \mu\text{m}^2/\text{s}$ for 500 kDa dextran.

While this diffusive model captures the basic exponential approach to equilibrium, it substantially underestimates the rate of solute accumulation observed in experiments (Fig. 1d). This suggests that another transport mechanism accelerates solute entry into the chamber.

Inclusion of diffusio-osmosis (DO)

The discrepancy can be explained by **diffusio-osmosis (DO)**—a convective flow of solvent along the channel walls driven by the solute concentration gradient in the connecting neck. Such flow moves solvent from the low-concentration chamber toward the high-concentration main

channel, while mass conservation induces a compensating backflow in the center of the channel that carries solute-rich fluid into the chamber.

To incorporate this effect, we retain the two-reservoir representation. Reservoir 1 is again treated as an infinite reservoir at constant concentration c_1, and Reservoir 2 as a finite cylindrical chamber with time-dependent average concentration $c_2(t)$. The local concentration at the channel entrance, c_{local}, evolves due to DO-driven solute transport across the neck.

The key assumption is that the incoming backflow carries solute at an average concentration $(c_1 + c_{\mathrm{local}})/2$, while the outgoing surface flow carries solute at concentration c_{local}. The resulting net solute flux is proportional to $(c_1 - c_{\mathrm{local}})/2$. Assuming a symmetric parabolic velocity profile, the volumetric flow rate is:

$$Q = \gamma\, v_{\mathrm{DO}}(c_{\mathrm{local}})\, w_n h_n, \qquad \gamma = \frac{1}{3\sqrt{3}},$$

leading to:

$$\frac{dc_{\mathrm{local}}}{dt} = \frac{1}{2 \cdot 3\sqrt{3}} \cdot \frac{w_n h_n}{V_2} v_{\mathrm{DO}}(c_{\mathrm{local}})(c_1 - c_{\mathrm{local}}).$$

The diffusio-osmotic slip velocity depends on the osmotic pressure difference between the main channel and the chamber entrance:

$$\Pi(c) = \Pi_0 \left(\frac{c}{c_0}\right)^n, \quad \Pi_0 = 20\ \mathrm{kPa},\ c_0 = 10\%,\ n = 2.5,$$

with an effective depletion layer thickness

$$\lambda(c) = \left(\frac{k_B T}{\Pi(c)}\right)^{1/3},$$

and

$$v_{\mathrm{DO}}(c) = \frac{\lambda^2(c)}{2\eta} \cdot \frac{\Pi(c_1) - \Pi(c)}{l_n}.$$

Inside the chamber, solute introduced by DO-driven backflow does not mix instantaneously but gradually homogenizes by molecular diffusion. We model this by relaxing the chamber-averaged concentration $c_2(t)$ toward c_{local} on a characteristic mixing timescale:

$$\frac{dc_2}{dt} = \frac{1}{\tau_{\mathrm{mix}}}(c_{\mathrm{local}} - c_2), \qquad \tau_{\mathrm{mix}} = \frac{h_c^2}{\pi^2 D}.$$

The coupled equations

$$\frac{dc_{\mathrm{local}}}{dt} = \frac{1}{2 \cdot 3\sqrt{3}} \cdot \frac{w_n h_n}{V_2} v_{\mathrm{DO}}(c_{\mathrm{local}})(c_1 - c_{\mathrm{local}}),$$

$$\frac{dc_2}{dt} = \frac{1}{\tau_{\mathrm{mix}}}(c_{\mathrm{local}} - c_2),$$

thus describe the combined influence of diffusio-osmotic transport through the neck and diffusive equilibration within the chamber.

Concentration calibration and details on dextran concentration control

To mitigate the impact of crosstalk between rhodamine and FITC dyes and to account for geometric deviation among different devices, it is imperative to divide the experiments into two separate trials while maintaining consistent dextran droplet concentrations on the same device1.

In each experiment, FITC-labeled PEG (0.1 wt% FITC) and FITC-labeled dextran (0.1 wt%FITC) are used individually. After filling the device with DI water, a 10 wt% dextran solution is introduced to the device, and sequential injections of 12 wt% PEG, 10 wt% PEG, 8 wt% G, 7 wt% PEG, and 6 wt% PEG, with each injection occurring at 5-hour intervals, are performed (Fig.S2a, b). To be able to adequately quantify the concentrations of dextran and PEG, we performed a calibration by measuring FITC intensities on samples of known concentrations in a confocal microscope (Leica, STELLARIS 5), shown in Fig.S2c, d. For calibration of the FITC-labeled dextran we use total dextran concentrations of 6 wt%, 8 wt%, 10 wt%, 12.5 wt%, 15 wt%, and 17.5 wt%; for the calibration of the FITC-labeled PEG, we use concentrations of 0.2 wt%, 0.5 wt%, 1 wt%, 2 wt%, and 3 wt%. After using ImageJ for analyzing the intensities in the acquired images, we obtain calibration curves for dextran and PEG by fitting the measured intensities as a function of concentration c as: $I_{dex}(c) = 1.49\ c - 2.26$ and $I_{PEG}(c) = 1.49\ c - 2.26$, respectively.

Data on dextran droplet size control

As shown in Fig.S4a, the geometry used in this work can be divided into four distinct zones. Within zone 1 to 3, the geometry is divided into eight regions, where each region exhibits a variation in the length of the connection neck, ranging from 60 µm to 360 µm at 50 µm intervals, while between each region, there is a variation in the width of the connection neck ranging from 30 µm to 100 µm at 10 µm intervals. Zone 4 consists of seven regions, which are ordered by connection neck length from 60 µm to 360 µm at 50 µm intervals; within each of these regions, the connection neck width is varied from 30 µm to 100 µm at 10 µm intervals. Using a custom MATLAB code to extract the size of each dextran droplet, we obtain a comprehensive analysis of the overall size variation, shown in Fig.S4b, c, d, which accounts for the impact of dextran diffusion time as well as the effects of connection neck length and width.

Fabrication of Inter-droplet communication devices

The femtosecond laser micromachining technique (FLM) provides a remarkable three-dimensional processing capability that enables the fabrication of complex and intricate microfluidic chips. To further highlight the potential applications of this method and the fabricated microfluidic chip, we demonstrate a communication microfluidic device created using FLM. The device employs our in-situ LLPS methodology for the controlled generation of two distinct types of droplets in two rows of dead-end chambers; chambers from the two rows can then be brought in contact with each other by opening integrated micro-valves built into the device. In our test experiments, we generate FITC-labeled droplets in one row and unlabeled droplets in the second row. The results of this experiment are presented in the main text and in Fig.S6a. The device consists of four main layers:

Layer 1 is a standard PDMS cover with five holes: two inlets for the formation of different types of dextran droplets, two outlets, and one inlet for pressure control.

Layer 2, is based on a 1 mm slide of fused silica glass; it comprises a series of micro valves connected to the main channel through corresponding connection necks. Pressure control is achieved through a single inlet. The microvalves are through holes with dimensions of 1 mm in depth and 0.6 mm in diameter. The depths of the main channel and the connection necks are maintained at 0.2 mm.

Layer 3 is a PDMS membrane of 150 µm thickness. It contains four through holes: two for the inlets and two for the outlets.
Layer 4, is based on a 1 mm slide of fused silica glass. This layer incorporates two independent droplet production systems, one for generating labeled dextran droplets and the other for producing unlabeled dextran droplets. Leveraging the powerful 3D processing capability of FLM, these two systems are positioned in parallel, with a 0.1 mm distance maintained between the series of chambers in each system (see Fig.S6b).
Once the four layers have been prepared and the corresponding holes have been aligned, the bonding process begins by joining layers 1, 2 and 3. Subsequently, a syringe connected to the pressure control inlet is utilized to create negative pressure, which causes deformation of the PDMS membrane upwards, into the "valves open" state. This negative pressure and the corresponding membrane state is maintained during the next bonding step, where layers 1-3 are bonded to layer 4 under a microscope (see Fig.S6c); this circumvents contact of the PDMS valve membranes to the surface of layer 4 during bonding. To further ensure that the valve membranes do not bond to the bottom glass surface, we mitigate the impact of plasma treatment on these membrane by flushing the device with deionized water. To do so, we inject two syringes filled with deionized (DI) water into the two inlets on the PDMS cover, thus reducing any residual effects from the plasma treatment.
In this work, the entire process is manually operated, and, as a result, the alignment of the valves with the two dead-end chambers may occasionally be misaligned. However, it is plausible to envision that an appropriate setup could automate the entire process and thus improve on the alignment and reproducibility of the device fabrication.

Comparison of Devices made by Soft Lithography and Femtosecond Laser Machining

To achieve a high-throughput dead-end chamber microfluidic chip, the most effective approach is to utilize the method of photolithography within a process termed Soft Lithography[2,3], as illustrated schematically in Fig.S7a. For the photolithography process, we selected SU-8 2075 as a photoresist layer, following the protocol recommended by the manufacturer (see data sheet provided by microchem inc.) to achieve a layer of around 200 µm thickness [4]. In the exposure step, we use a photomask photomask printed at SELBA S.A., Geneva, Switzerland.
After completing the photolithography process, we proceed with a PDMS moulding process. Initially, PDMS is poured onto the prepared photoresist mould, followed by vacuum filling of PDMS into the mould. The sample is then placed in an oven and cured at 65 oC. Then, a cover glass is plasma bonded onto the prepared PDMS open channel. Through the standard Soft Lithography technique, a PDMS-based microfluidic chip integrating hundreds or thousands of dead-end geometries can thus be rapidly realized. For an example device, see Fig.S7c
The geometry of the PDMS-based microfluidic chip used in this study is similar to the fused silica-based microfluidic chip, with the main channel width remaining constant at 200 µm. However, each chamber's diameter is 100 µm, which is smaller than for the fused silica device. This reduction in diameter enables the integration of a greater number of dead-end geometries on a single slide (75 mm x 25 mm). However, due to the limitations of the soft lithography process, it is difficult to achieve a total depth of the structures on a device that exceeds 300 µm. The PDMS-based device used here exhibits a depth of around 200 µm.

Moreover, comparing these two types of microfluidic chip in terms of absorption of small molecules into the bulk of the device, we observe a significant absorption effect in PDMS-based devices, whereas the glass-based devices do not display any measurable absorption, as shown in the comparison in Fig.S7d.

We also find that large coacervate droplets cannot be readily produced in a PDMS-based microfluidic chip, as shown in Fig.S7f, due to the small formed coacervate droplets sticking to the PDMS surface.

Nevertheless, we find that the PDMS-based devices still enable an accurate control of the concentration in the chambers. To further validate the process, we perform numerical simulations using COMSOL, which indicate that different flow rates in the main channel have a negligible effect on the final concentration in the dead-end chambers (see Fig.S7e). This suggests that our method is robust with respect to the flow rates applied in the main channel and does not require precise flow rate control to enable a controlled W/W droplet generation. This applies to both glass devices as well as PDMS-based microfluidic devices.

Coacervates in different salt concentrations and formation of single coacervate droplets

In addition to the conditions described in the main text, we study a wider range of KCl concentrations (0.1–1.0 M) to investigate coacervate behavior. At low salt concentrations, we observe the formation of micron-sized coacervates, which appear as dark regions in the chambers. As the salt concentration increases, the coacervates appear brighter, indicating the merging of smaller droplets into larger ones (see Fig. S8a). We capture and analyze this process using 20× magnification images at salt concentrations of 0.4 M, 0.6 M, 0.8 M, and 1.0 M (see Fig. S8a). Even at 1.0 M, the coacervates persist as dispersed droplets due to the long relaxation time of polymer chains.

To accelerate the merging process, we construct a centrifugal device with a 20 cm diameter disc. Centrifugation at 600 rpm for approximately 2 hours concentrates the droplets at the edges of the chambers. However, significant time is still required to achieve the formation of a single coacervate droplet (see Fig. S8b).

A minimal two-compartment diffusion model for droplet–droplet communication

Communication between two droplets confined in neighboring dead-end chambers is mediated by diffusive transport through an interconnecting channel controlled by a pneumatic valve. The valve switches the connection between on (open) and off (closed).

We adopt a minimal lumped description:

1. Each droplet (or the droplet plus its associated confined aqueous volume) is treated as a well-mixed compartment with finite effective volume $V_1$and V_2.
2. Exchange is diffusion-dominated through the connection; convective contributions are neglected.
3. Fluorescence intensity in each droplet is proportional to the average tracer concentration in that droplet after background subtraction.

Let $C_L(t)$and $C_U(t)$denote the average tracer concentrations in the labelled droplet and the unlabeled droplet, respectively. When the valve is open, the diffusive flux through the connection is

$J = G\,(C_L - C_U)$,

$$G = \frac{D_{eff} A_{eff}}{L},$$

where D_{eff} is an effective diffusion coefficient, A_{eff} is the valve-controlled effective open area, and L is the effective diffusion length.

Mass conservation for the two compartments gives:

$$V_L \frac{dC_L}{dt} = -G(C_L - C_U),$$

$$V_U \frac{dC_U}{dt} = +G(C_L - C_U).$$

When the valve is closed, $A_{eff} \approx 0 \Rightarrow G \approx 0$, and the concentrations remain (approximately) constant.

Define the concentration difference $\Delta C(t) = C_L(t) - C_U(t)$. Then

$$\frac{d\Delta C}{dt} = -G\left(\frac{1}{V_L} + \frac{1}{V_U}\right)\Delta C,$$

leading to an exponential relaxation

$$\Delta C(t) = \Delta C(0)\exp\left(-\frac{t}{\tau}\right),$$

$$where\ \tau = \left[G\left(\frac{1}{V_L} + \frac{1}{V_U}\right)\right]^{-1}.$$

The total tracer amount is conserved, hence

$$V_L C_L(t) + V_U C_U(t) = V_L C_L(0) + V_U C_U(0).$$

Thus, both droplets relax towards a common equilibrium concentration

$$C_\infty = \frac{V_L C_L(0) + V_U C_U(0)}{V_L + V_U}.$$

After background subtraction, fluorescence intensities are proportional to concentrations, as

$$I_L(t) - I_{bg} = \alpha\, C_L(t)\ , and$$

$$I_U(t) - I_{bg} = \alpha\, C_U(t).$$

Therefore, the metric plotted in Fig. 5b,

$$R(t) = \frac{I_{unlabelled}(t)}{I_{labelled}(t)} \approx \frac{C_U(t)}{C_L(t)},$$

monotonically increases over time as tracer molecules diffuse from the labelled droplet to the unlabelled droplet. In the symmetric case ($V_L \approx V_U$, $C_U(0) \approx 0$), $R(t)$increases from 0 and approaches 1 as the two droplets equilibrate.

Within this model, the "communication intensity" is naturally quantified by $1/\tau$, which depends on the effective diffusive conductance $G \propto A_{eff}$. Thus, valve closure corresponds to $G \approx 0$ (communication off), valve opening corresponds to $G = G_{open}$(communication on), and partial opening enables continuous modulation of the communication rate.

Based on this simple model, we estimated several parameters in our communication system, as

- $D_{eff} = 13.7\ \mu m^2/s$
- $A_{eff} = 800\ \mu m^2$
- $L = 800\ \mu m$
- $V_L = V_U = 10\ nL$

Based on these parameters, we obtain $G \approx 13.7\ \mu m^3/s$, and $\tau \approx 101\ h$.

In Fig. 5b, the experimentally measured ratio reaches $R(t) \approx 0.4$ after 48 h, which is in close agreement with the simple model prediction $t/\tau \approx 48/101 \approx 0.47$ obtained using representative geometric and transport parameters. This quantitative consistency supports the validity of the diffusion-based two-compartment model in capturing the essential features of the droplet–droplet communication dynamics. The remaining discrepancy can be primarily attributed to uncertainty in the effective diffusive area A_{eff}, which is sensitive to fabrication- and operation-related factors, including layer-to-layer alignment tolerances, the thickness of the intermediate PDMS membrane, and the magnitude of the applied negative pneumatic pressure. These factors introduce variability in the actual interconnecting cross-section but do not alter the underlying diffusion-limited mechanism described by the model.

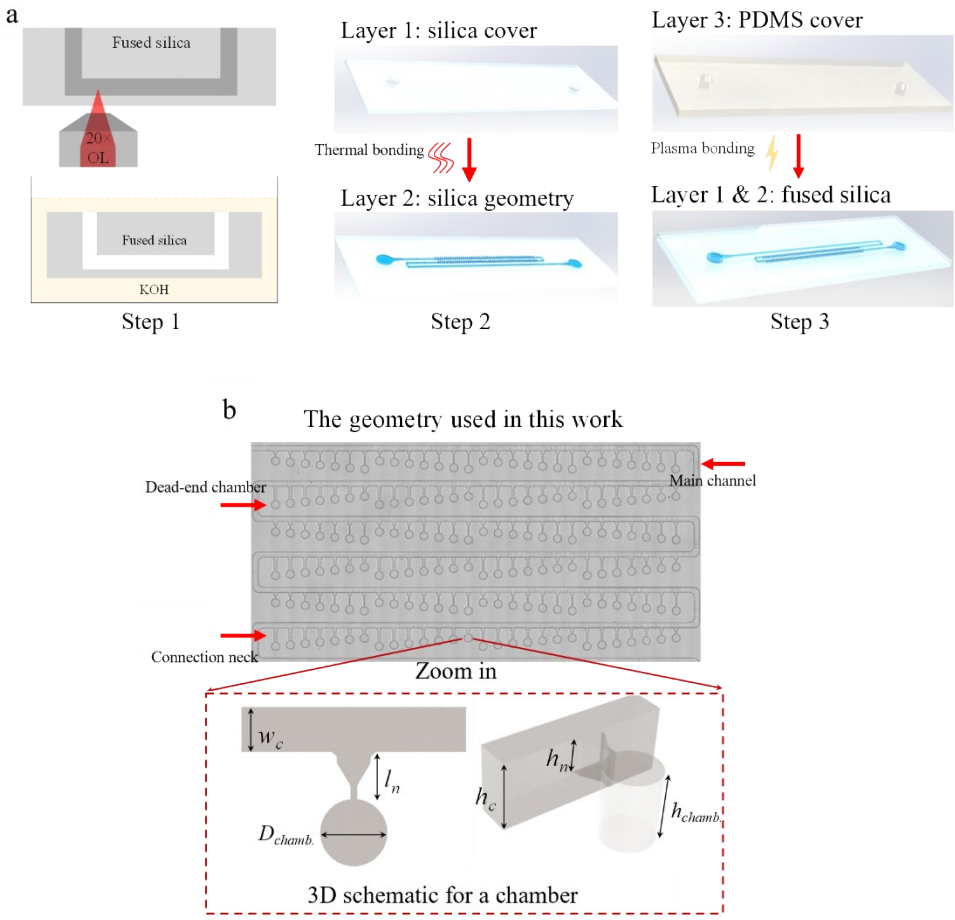

Fig. S1. Fabrication flow chart and geometry of the fused silica microfluidic chip used in this study. a, Schematic representation of three steps for device fabrication, step 1: Femtosecond laser micromachining (FLM); step 2: Thermal bonding of two silica layers at 1000 °C for 72 hours or at 1200 °C for 10 hours; step 3: Plasma bonding of a PDMS cover onto the fused silica layer. b, Tile-scanning image of the whole geometry captured by confocal microscope and schematic of the three-dimensional structure of the dead-end chambers utilized in this study.

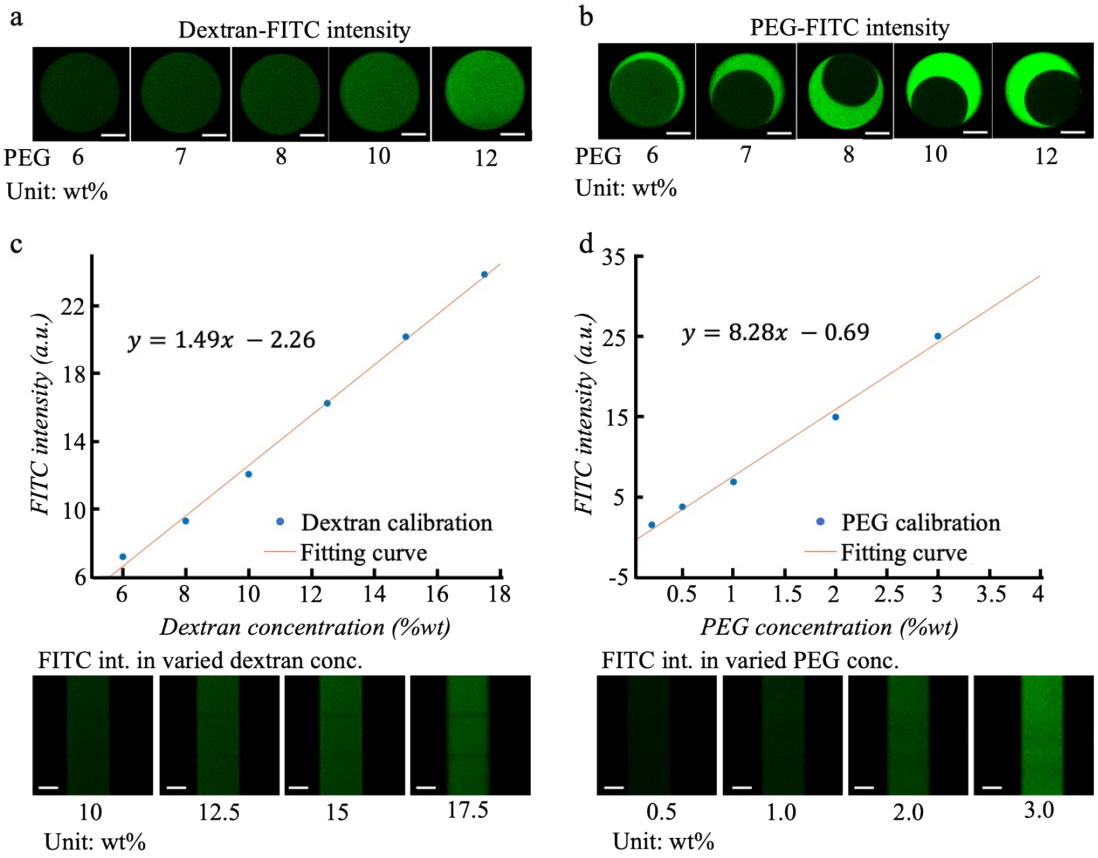

Fig. S2. Dextran droplets concentration control and concentration calibration curves for the dextran-PEG solution. a, Development of dextran-FITC fluorescent intensity for different PEG concentrations. Scale bar is 100 µm. b, A separate experiment shows the development of PEG-FITC intensity surrounding a dextran droplet scale bar 100 µm. c, Calibration curve depicting the relationship between concentration and fluorescence intensity for FITC-labelled dextran. d, Calibration curve illustrates the correlation between concentration and fluorescence intensity for FITC-labelled PEG. Scale bar 100 µm.

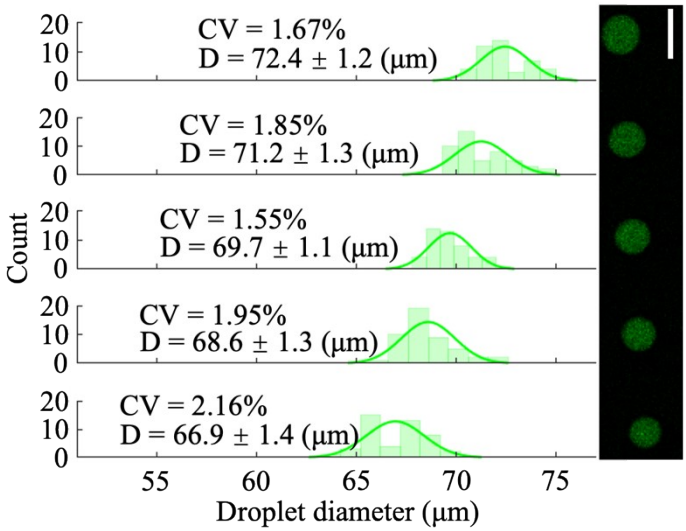

Fig. S3. The diameter distribution in five different kinds of dead-end chambers, counting 45 chambers for each statistic. Scale bar 100 μm.

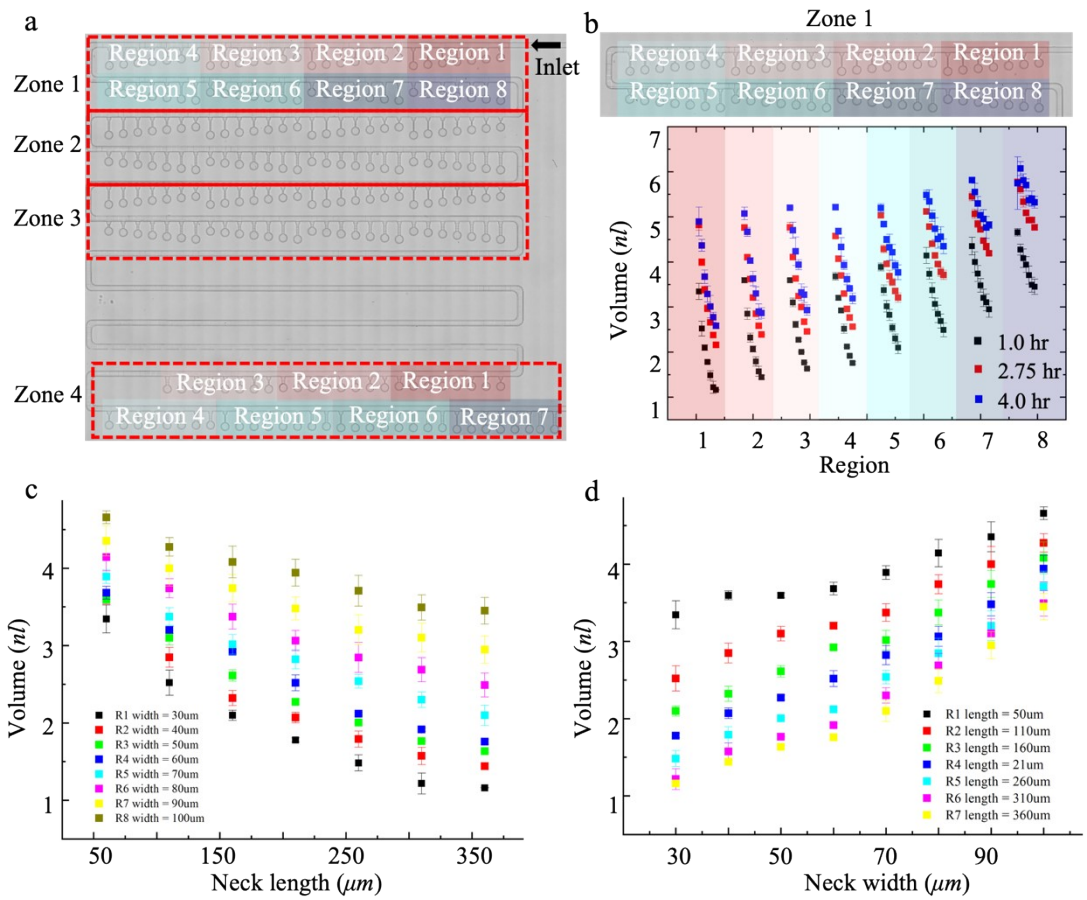

Fig. S4. Variation analysis of dextran droplet volumes through a custom MATLAB code. a, The geometry was divided into four zones. Zones 1-3 have eight regions with the connection neck length varied in each region. Zone 4 has seven regions with a connection neck width different in each region. b, Evolution of droplet volumes in each region by applying three different dextran diffusion times (1 hour, 2.75 hours and 4 hours), corresponding to black, red, and blue square dots, same color represents the same geometry. c, Variation in droplet volumes in each region corresponds to different connection neck lengths, with the same color representing the same connection neck width. d, Variation in droplet volumes in each region corresponds to different connection neck widths, with the same color indicating the same connection neck length.

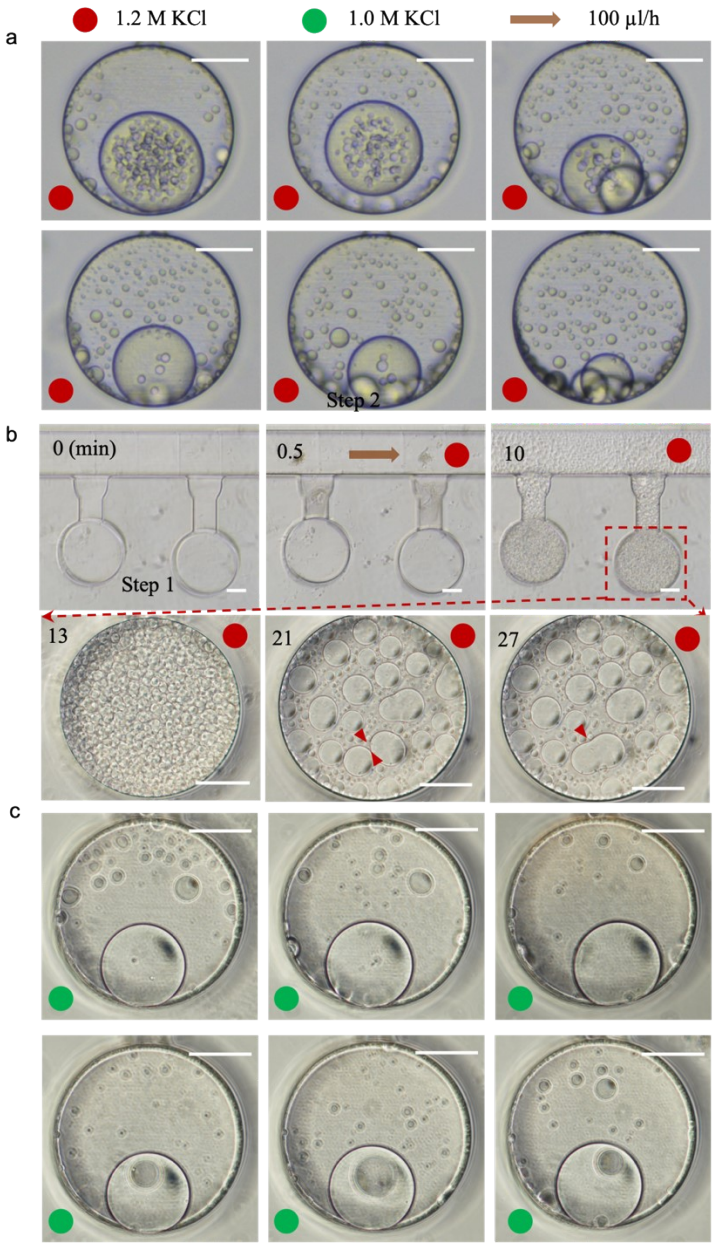

Fig. S5. Compartmentalization in different sizes of coacervate droplets and the corresponding final equilibrium states. a, More multiple compartments form in larger coacervates droplets. b, Generation of coacervates in the dead-end chamber without the assistance of gravity. c, Some stable coacervates droplets form in 1 M KCl medium after 2 days. Scale bars are 100 µm.

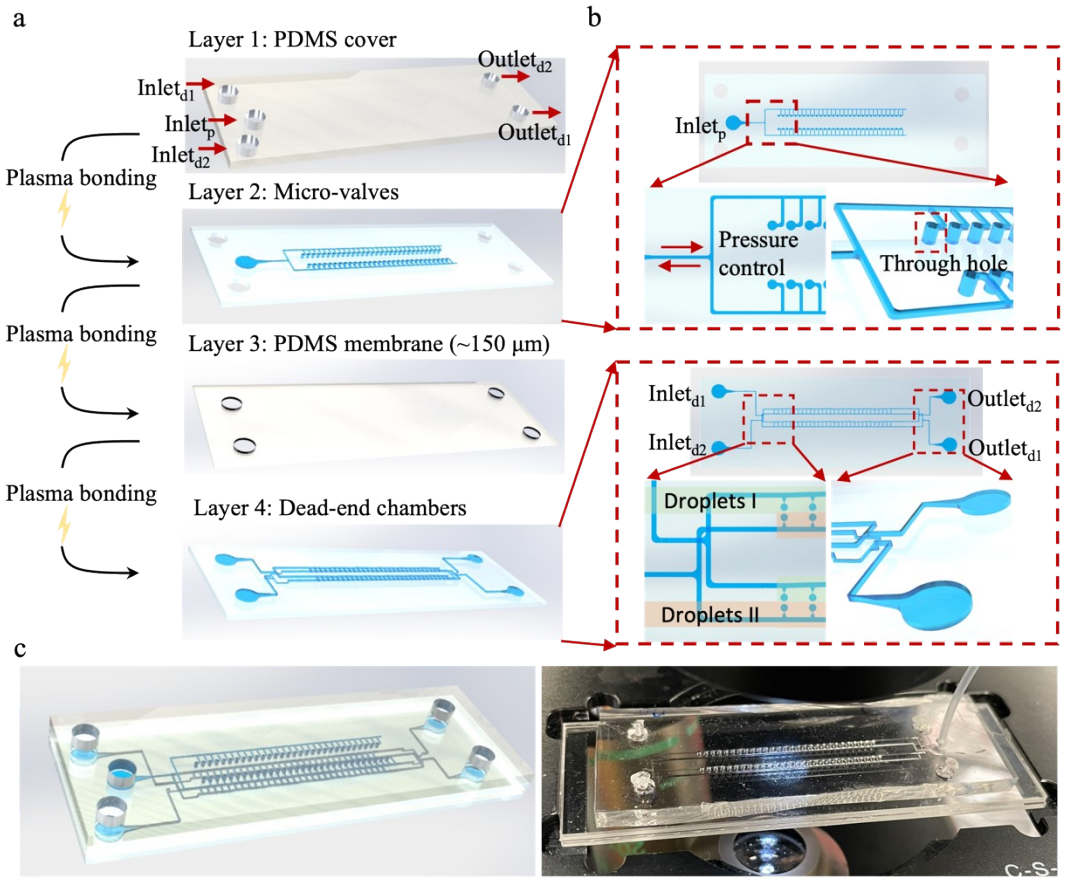

Fig. S6. Schematic flow chart and structural details of the communication microfluidic chip. a, The communication microfluidic chip comprises four layers: a PDMS cover for inlet/outlet, a fused silica micro-valve layer, a PDMS membrane, and fused silica dead-end chambers. b, Detailed depiction of the structure, including the fused silica micro-valves and the fused silica dead-end chambers. c, Schematic and photo of the chip after assembly.

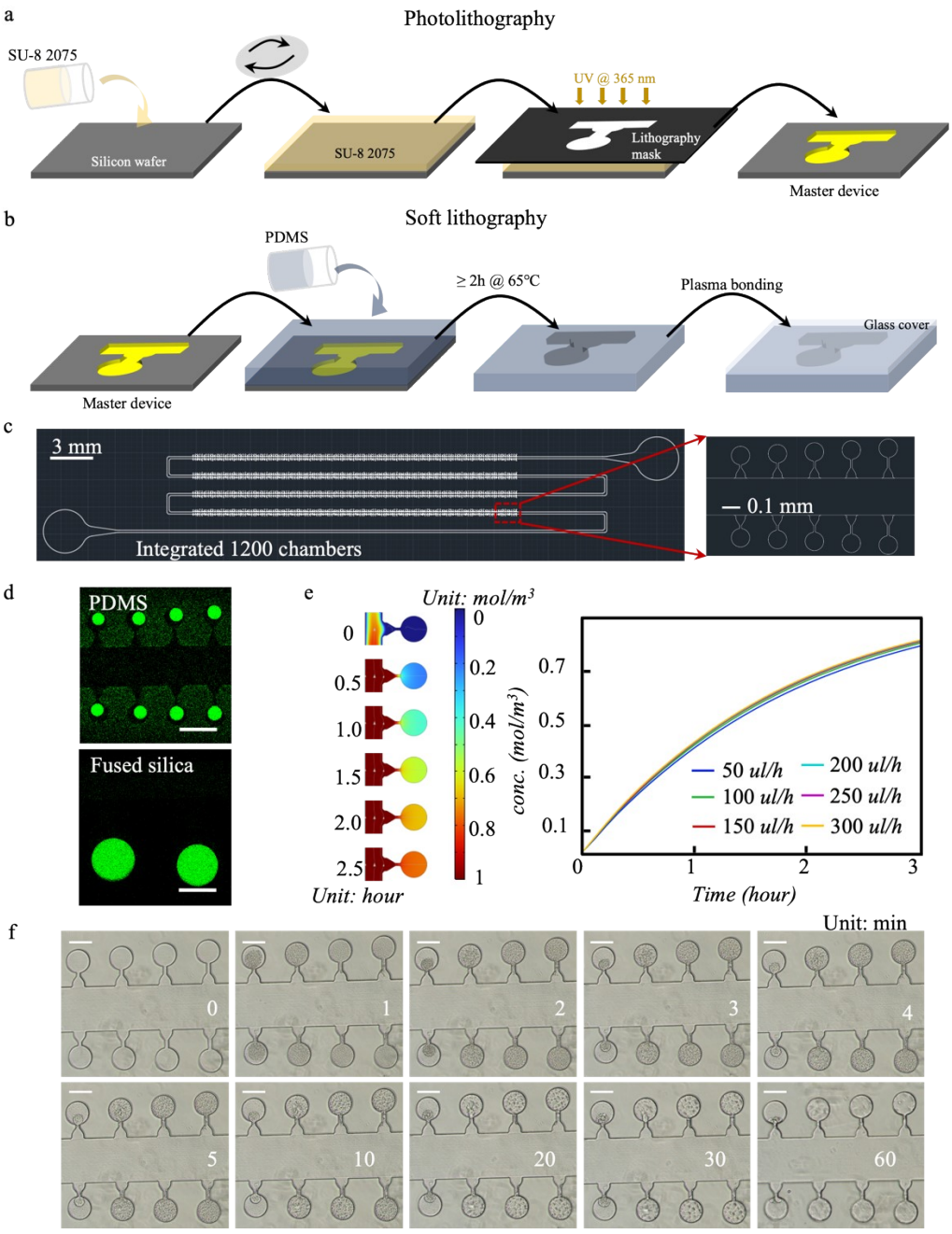

Fig. S7. Comparison of PDMS-based microfluidic chip realized by soft photolithography (SPL) with silica-based microfluidic chip realized by FLM. a, Schematic flow chart illustrating the fabrication process of photolithography (PL). b, Schematic flow chart illustrating the fabrication process of soft lithography (SL). c, Masks utilized for SPL, integrating 1200 dead-end chambers, along with a detailed view of their zoomed-in geometries. d, Comparison of the absorption effect in PDMS-based and fused silica-based microfluidic chips. Scale bars are 100 μm. e, Comsol simulation of the effect of different flow rates in the main channel on matter concentration in a dead-end chamber. f, Coacervate droplets cannot be produced in a PDMS-based microfluidic chip. Scale bars are 100 μm.

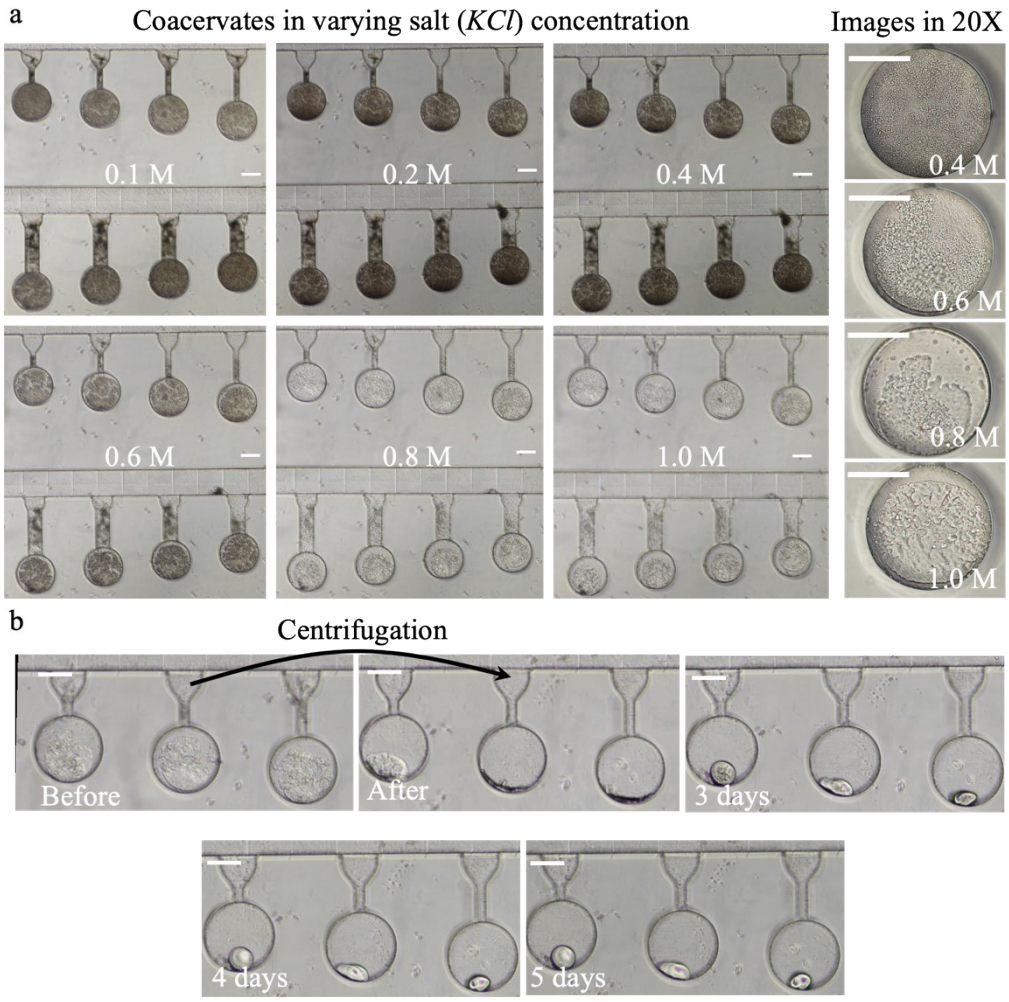

Fig. S8. Development of coacervates from low to high salt (KCl) concentrations and the centrifugation method for condensing coacervates. a, Evolution of coacervates from 0.1 M to 1.0 M KCl solution and images displaying the state of coacervates at 0.6 M, 0.8 M, and 1.0 M KCl concentrations captured by using a 20X lens. b, Utilization of the centrifugation method for condensing complex coacervates, with a visual representation of their development over 5 days. Scale bars are 100 μm.

Movie S1 (SI_Movie_01). Diffusion of fluorescently labeled dextran into dead-end chambers. This movie shows the diffusion of 10 wt% dextran, labeled with green dye (FITC), into dead-end chambers. The fluorescence intensity reflects the dextran concentration, demonstrating how diffusion between the main channel and chambers controls the concentration in each chamber.

Movie S2 (SI_Movie_02). Formation of dextran droplets triggered by injection of 10 wt% PEG. This movie shows the formation of dextran droplets when 10 wt% PEG, labeled with red dye (rhodamine), is injected into the device, inducing liquid-liquid phase separation. The flow rate in the main channel is maintained at 100 μL/h.

Movie S3 (SI_Movie_03). 3D fluorescent imaging of dextran droplet formation. This movie shows a 3D fluorescent view of dextran droplet formation in the dead-end chambers. Dextran is labeled with green dye, while PEG is labeled with red dye.

Movie S4 (SI_Movie_04). Bright field view of dextran droplet formation. This movie shows the dextran droplet formation process observed under a bright-field microscope after the injection of 10 wt% PEG into the device.

Movie S5 (SI_Movie_05). Droplet response to increase of PEG concentration from 6 wt% to 7 wt%. This movie shows the development of dextran droplets after the PEG concentration in the main channel has been increased from 6 wt% to 7 wt%.

Movie S6 (SI_Movie_06). Droplet response to increase of PEG concentration from 7 wt% to 8 wt%. This movie shows the development of dextran droplets after the PEG concentration in the main channel has been increased from 7 wt% to 8 wt%.

Movie S7 (SI_Movie_07). Droplet response to increase of PEG concentration from 8 wt% to 10 wt%. This movie shows the development of dextran droplets after the PEG concentration in the main channel has been increased from 8 wt% to 10 wt%.

Movie S8 (SI_Movie_08). Droplet response to increase of PEG concentration from 10 wt% to 12 wt%. This movie shows the development of dextran droplets after the PEG concentration in the main channel has been increased from 10 wt% to 12 wt%.

SI References

1. Wei He, H. W., Lynn C. Hartmann, Ji-Xin Cheng, and Philip S. Low. In vivo quantitation of rare circulating tumor cells by multiphoton intravital flow cytometry. Proceedings of the National Academy of Sciences 104, 5 (2007).
2. Lin, Y., Gao, C., Gritsenko, D., Zhou, R. & Xu, J. Soft lithography based on photolithography and two-photon polymerization. Microfluidics and Nanofluidics 22, doi:10.1007/s10404-018-2118-5 (2018).
3. Kavand, H. et al. Cell-Imprint Surface Modification by Contact Photolithography-Based Approaches: Direct-Cell Photolithography and Optical Soft Lithography Using PDMS Cell Imprints. ACS Appl Mater Interfaces 11, 10559-10566, doi:10.1021/acsami.9b00523 (2019).
4. Data sheet provided by microchem inc.